# Searching for Heavy Dark Matter near the Planck Mass with XENON1T

E. Aprile,[1] K. Abe,[2] S. Ahmed Maouloud,[3] L. Althueser,[4] B. Andrieu,[3] E. Angelino,[5] J. R. Angevaare,[6] V. C. Antochi,[7] D. Antón Martin,[8] F. Arneodo,[9] L. Baudis,[10] A. L. Baxter,[11] M. Bazyk,[12] L. Bellagamba,[13] R. Biondi,[14] A. Bismark,[10] E. J. Brookes,[6] A. Brown,[15] S. Bruenner,[6] G. Bruno,[12] R. Budnik,[16] T. K. Bui,[2] C. Cai,[17] J. M. R. Cardoso,[18] D. Cichon,[14] A. P. Cimental Chavez,[10] M. Clark,[11] A. P. Colijn,[6] J. Conrad,[7] J. J. Cuenca-García,[10] J. P. Cussonneau,[12,*] V. D'Andrea,[19,†] M. P. Decowski,[6] P. Di Gangi,[13] S. Di Pede,[6] S. Diglio,[12] K. Eitel,[20] A. Elykov,[20] S. Farrell,[21] A. D. Ferella,[22,19] C. Ferrari,[19] H. Fischer,[15] M. Flierman,[6] W. Fulgione,[5,19] C. Fuselli,[6] P. Gaemers,[6] R. Gaior,[3] A. Gallo Rosso,[7] M. Galloway,[10] F. Gao,[17] R. Glade-Beucke,[15] L. Grandi,[8] J. Grigat,[15] H. Guan,[11] M. Guida,[14] R. Hammann,[14] A. Higuera,[21] C. Hils,[23] L. Hoetzsch,[14] N. F. Hood,[24] J. Howlett,[1] M. Iacovacci,[25] Y. Itow,[26] J. Jakob,[4] F. Joerg,[14] A. Joy,[7] N. Kato,[2] M. Kara,[20] P. Kavrigin,[16] S. Kazama,[26] M. Kobayashi,[26] G. Koltman,[16] A. Kopec,[24] F. Kuger,[15] H. Landsman,[16] R. F. Lang,[11] L. Levinson,[16] I. Li,[21] S. Li,[11,‡] S. Liang,[21] S. Lindemann,[15] M. Lindner,[14] K. Liu,[17] J. Loizeau,[12] F. Lombardi,[23] J. Long,[8] J. A. M. Lopes,[18,§] Y. Ma,[24] C. Macolino,[22,19] J. Mahlstedt,[7] A. Mancuso,[13] L. Manenti,[9] F. Marignetti,[25] T. Marrodán Undagoitia,[14] K. Martens,[2] J. Masbou,[12] D. Masson,[15] E. Masson,[3] S. Mastroianni,[25] M. Messina,[19] K. Miuchi,[27] K. Mizukoshi,[27] A. Molinario,[5] S. Moriyama,[2] K. Morå,[1] Y. Mosbacher,[16] M. Murra,[1] J. Müller,[15] K. Ni,[24] U. Oberlack,[23] B. Paetsch,[16] J. Palacio,[14] Q. Pellegrini,[3] R. Peres,[10] C. Peters,[21] J. Pienaar,[8] M. Pierre,[6,12] V. Pizzella,[14] G. Plante,[1] T. R. Pollmann,[6] J. Qi,[24] J. Qin,[11] D. Ramírez García,[10] R. Singh,[11] L. Sanchez,[21] J. M. F. dos Santos,[18] I. Sarnoff,[9] G. Sartorelli,[13] J. Schreiner,[14] D. Schulte,[4] P. Schulte,[4] H. Schulze Eißing,[4] M. Schumann,[15] L. Scotto Lavina,[3] M. Selvi,[13] F. Semeria,[13] P. Shagin,[23] S. Shi,[1] E. Shockley,[24] M. Silva,[18] H. Simgen,[14] A. Takeda,[2] P.-L. Tan,[7] A. Terliuk,[14,‖] D. Thers,[12] F. Toschi,[20,15] G. Trinchero,[5] C. Tunnell,[21] F. Tönnies,[15] K. Valerius,[20] G. Volta,[10] C. Weinheimer,[4] C. Wittweg,[10] T. Wolf,[14] V. H. S. Wu,[20] Y. Xing,[12] D. Xu,[1] Z. Xu,[1] M. Yamashita,[2] L. Yang,[24] J. Ye,[1] L. Yuan,[8] G. Zavattini,[28] M. Zhong,[24] and T. Zhu[1]

(XENON Collaboration)[¶]

[1]*Physics Department, Columbia University, New York, New York 10027, USA*
[2]*Kamioka Observatory, Institute for Cosmic Ray Research, and Kavli Institute for the Physics and Mathematics of the Universe (WPI), University of Tokyo, Higashi-Mozumi, Kamioka, Hida, Gifu 506-1205, Japan*
[3]*LPNHE, Sorbonne Université, CNRS/IN2P3, 75005 Paris, France*
[4]*Institut für Kernphysik, Westfälische Wilhelms-Universität Münster, 48149 Münster, Germany*
[5]*INAF-Astrophysical Observatory of Torino, Department of Physics, University of Torino and INFN-Torino, 10125 Torino, Italy*
[6]*Nikhef and the University of Amsterdam, Science Park, 1098XG Amsterdam, Netherlands*
[7]*Oskar Klein Centre, Department of Physics, Stockholm University, AlbaNova, Stockholm SE-10691, Sweden*
[8]*Department of Physics and Kavli Institute for Cosmological Physics, University of Chicago, Chicago, Illinois 60637, USA*
[9]*New York University Abu Dhabi—Center for Astro, Particle and Planetary Physics, Abu Dhabi, United Arab Emirates*
[10]*Physik-Institut, University of Zürich, 8057 Zürich, Switzerland*
[11]*Department of Physics and Astronomy, Purdue University, West Lafayette, Indiana 47907, USA*
[12]*SUBATECH, IMT Atlantique, CNRS/IN2P3, Université de Nantes, Nantes 44307, France*
[13]*Department of Physics and Astronomy, University of Bologna and INFN-Bologna, 40126 Bologna, Italy*
[14]*Max-Planck-Institut für Kernphysik, 69117 Heidelberg, Germany*
[15]*Physikalisches Institut, Universität Freiburg, 79104 Freiburg, Germany*
[16]*Department of Particle Physics and Astrophysics, Weizmann Institute of Science, Rehovot 7610001, Israel*
[17]*Department of Physics and Center for High Energy Physics, Tsinghua University, Beijing 100084, China*
[18]*LIBPhys, Department of Physics, University of Coimbra, 3004-516 Coimbra, Portugal*
[19]*INFN-Laboratori Nazionali del Gran Sasso and Gran Sasso Science Institute, 67100 L'Aquila, Italy*
[20]*Institute for Astroparticle Physics, Karlsruhe Institute of Technology, 76021 Karlsruhe, Germany*
[21]*Department of Physics and Astronomy, Rice University, Houston, Texas 77005, USA*
[22]*Department of Physics and Chemistry, University of L'Aquila, 67100 L'Aquila, Italy*
[23]*Institut für Physik and Exzellenzcluster PRISMA⁺, Johannes Gutenberg-Universität Mainz, 55099 Mainz, Germany*
[24]*Department of Physics, University of California San Diego, La Jolla, California 92093, USA*
[25]*Department of Physics "Ettore Pancini," University of Napoli and INFN-Napoli, 80126 Napoli, Italy*
[26]*Kobayashi-Maskawa Institute for the Origin of Particles and the Universe, and Institute for Space-Earth Environmental Research, Nagoya University, Furo-cho, Chikusa-ku, Nagoya, Aichi 464-8602, Japan*

[27]*Department of Physics, Kobe University, Kobe, Hyogo 657-8501, Japan*
[28]*INFN—Ferrara and Dipartimento di Fisica e Scienze della Terra, Università di Ferrara, 44122 Ferrara, Italy*

Multiple viable theoretical models predict heavy dark matter particles with a mass close to the Planck mass, a range relatively unexplored by current experimental measurements. We use 219.4 days of data collected with the XENON1T experiment to conduct a blind search for signals from multiply interacting massive particles (MIMPs). Their unique track signature allows a targeted analysis with only 0.05 expected background events from muons. Following unblinding, we observe no signal candidate events. This Letter places strong constraints on spin-independent interactions of dark matter particles with a mass between $1 \times 10^{12}$ and $2 \times 10^{17}$ GeV/$c^2$. In addition, we present the first exclusion limits on spin-dependent MIMP-neutron and MIMP-proton cross sections for dark matter particles with masses close to the Planck scale.

Despite numerous pieces of evidence for dark matter (DM) and decades of dedicated searches, the nature of DM remains a mystery [1]. A wide class of production mechanisms predicts DM candidates near the Planck mass ($\simeq 10^{19}$ GeV/$c^2$), such as nonstandard thermal freeze-out [2,3], thermal freeze-in [4,5], first-order phase transitions [6,7], decays of heavy fields [8,9], gravitational particle production [10,11], and primordial black holes [12,13]. DM candidates in this mass range are less constrained by experiments and too heavy to be produced at colliders.

There has been a growing interest search for such heavy DM candidates [14], where new detection constraints have been explored considering spin-independent (SI) scattering. Assuming coherent interaction with a nucleus of mass number $A$, there is an $A^4$-enhanced sensitivity in SI scattering [15,16]. Xenon, with its large mass number, particularly benefits from this enhancement. However, the spin-dependent (SD) channel lacks experimental constraints, with the exception of an early study [17]. Xenon experiments can set leading SD constraints using the naturally abundant isotopes with nonzero nuclear spin [18,19].

Under the assumption of the standard halo model [20], the total DM flux decreases with particle mass due to the fixed local DM mass density [21], which predicts $\mathcal{O}(1)$event/(m$^2 \times$ yr) for Planck mass DM [22]. Thus, terrestrial direct detection experiments become flux limited. Although it is unlikely to generate the characteristic single-scatter pattern in a typical weakly interacting massive particles (WIMP) search, a heavy DM particle with a large cross section will generate a distinctive signal of multiple scatterings in the detector [23]. Therefore, to extend the experimental sensitivity to the highest mass near the Planck scale, analyses focusing on the multiple-scattering DM are

required. In this Letter, we present a dedicated analysis searching for multiply interacting massive particles (MIMPs) [23,24] for both SI and SD interactions in the XENON1T experiment [19,25]. The XENON1T experiment employs a dual-phase time projection chamber (TPC) with 2 tonnes of ultrapure liquid xenon in the target volume, located at INFN Laboratori Nazionali del Gran Sasso (LNGS) under 3600 m water-equivalent overburden [26].

It is common practice to report the cross sections for the SI, SD-neutron, and SD-proton interactions separately [27]; although an actual MIMP, denoted as $\chi$, could undergo all three interactions concurrently. The connection between the SI and SD interaction cross sections is model dependent, with some models predicting SD interactions being more easily accessible experimentally [28]. For SI scattering, the differential MIMP-nucleus scattering cross section $d\sigma_{A,\chi}^{\mathrm{SI}}/dq^2$ as a function of momentum transfer $q$ is

$$\frac{d\sigma_{A,\chi}^{\mathrm{SI}}}{dq^2} = \frac{\mu_{A,\chi}^2}{\mu_{\mathrm{nucleon},\chi}^2} A^2 |F_A(q)|^2 \sigma_{\mathrm{nucleon},\chi}^{\mathrm{SI}}, \qquad (1)$$

where $\sigma_{\mathrm{nucleon},\chi}^{\mathrm{SI}}$ is the total MIMP-nucleon scattering cross section. The Helm form factor $F_A(q)$ [29,30] is an approximation of the xenon nuclear structure functions, which is in good agreement with the calculations using large-scale shell models [31–33]. The squared ratio of the reduced MIMP-nucleus and MIMP-nucleon masses $\mu_{A,\chi}^2/\mu_{\mathrm{nucleon},\chi}^2$ is approximated to $A^2$ for $m_\chi \gg m_A$, which yields the $A^4$ enhancement for coherent SI scattering. However, this enhancement may not be universal at cross sections above $10^{-32}$ cm$^2$ [16]. We thus also report a conservative result by setting $\mu_{A,\chi}^2/\mu_{\mathrm{nucleon},\chi}^2 A^2$ to 1 in Eq. (1).

For SD scattering [34], the interaction can be described by the axial-vector–axial-vector Lagrangian. The SD interaction can be dominant if the SI interactions are either absent or strongly suppressed [28]. The differential MIMP-nucleon cross section $d\sigma_{A,\chi}^{\mathrm{SD}}/dq^2$ can then be written as a function of the total scattering cross section $\sigma_{n/p,\chi}^{\mathrm{SD}}$ between a MIMP and a single neutron or proton,

$$\frac{d\sigma_{A,\chi}^{SD}}{dq^2} = \frac{4}{3}\frac{\pi}{2J+1}\frac{\mu_{A,\chi}^2}{\mu_{n/p,\chi}^2}S_A^{a_0=1,a_1=\mp 1}(q)\sigma_{n/p,\chi}^{SD}, \quad (2)$$

with $\mu$ being the reduced masses, and $J$ being the initial ground-state angular momentum of the nucleus. Here, the axial-vector structure function $S_A(q)$ [35] follows the definition in Ref. [19]. For comparison across different target materials, experimental results are conventionally reported in the special cases of "neutron-only" ("proton-only") coupling, where for $S_A(q)$, its isoscalar term $a_0 = 1$, and its isovector term $a_1 = -1$ (1). The xenon used in XENON1T contains two isotopes with nonzero nuclear spin, $^{129}$Xe (spin 1/2) and $^{131}$Xe (spin 3/2), with abundances measured to be 26.4% and 21.2%, respectively, with <1% uncertainty [19]. We report our results using the $S_A(q)$ of the two xenon isotopes following the calculations by Menendez *et al.* [35], Klos *et al.* [36], Ressell and Dean [37], and Toivanen *et al.* [38].

Here we consider a MIMP with a mass above $10^{12}$ GeV/$c^2$, such that each scattering causes negligible deviation from its path, and all recoils are aligned in a collinear track in the TPC [23,24]. We calculate the energy loss of such a MIMP in Earth's overburden before reaching the detector, by accounting for Earth's composition [36,39] and isotope abundances [24]. We find the energy loss from the shielding is less than 0.1% for the MIMP parameter space considered in this Letter (discussed below); hence we neglect the correction on the MIMP energy and flux due to their propagation through Earth. Details about this calculation are provided in the Appendix.

At Galactic speeds (~230 km/s), the median MIMP passage time through the XENON1T TPC is $\mathcal{O}(1)$ μs. Thus, scintillation (S1) signals from a MIMP track will merge into a single pulse of that timescale. The data processor for XENON1T [40] will misidentify such a wide pulse as an ionization (S2) signal, since the merged pulse lacks the canonical single-scatter S1 structure of a single maximum with a decay [26]. For clarity, we will refer to such merged pulses as a $S1_m$ pulse, which is a smoking-gun signature for MIMPs. After an initial $S1_m$ pulse, electrons freed from multiple spatially separated recoil sites will be drifted to the xenon gas to create a chain of multiple S2s. These will be reconstructed as one or more large S2 pulses, depending on the angle of the MIMP track through the TPC.

As described in Ref. [23], we simulate MIMP tracks isotropically from a sphere that encloses the detector. The velocity $\vec{v}$ of the MIMP is selected with a standard isothermal DM halo velocity distribution converted to the lab frame, denoted as $f(\vec{v})$, which is parameterized as in Ref. [25]. For each MIMP track across the detector, we define the per-meter nuclear recoil (NR) multiplicity as $\lambda$,

$$\lambda = n_{Xe}\int d\vec{v}\int dq^2 \frac{d\sigma_{A,\chi}}{dq^2}f(\vec{v}), \quad (3)$$
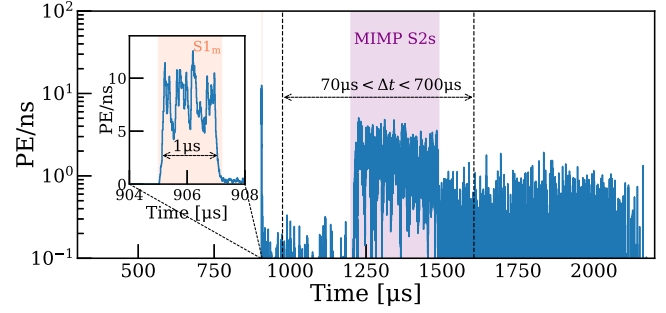


FIG. 1. An example waveform of a simulated MIMP interaction in XENON1T. The simulated spin-independent scattering cross section is $10^{-29}$ cm$^2$, corresponding to a NR rate of 500 per-meter track ($\lambda = 500$ NRs/m). The pulse in the orange band (enlarged in the inset) is the $S1_m$ signal. The pulses in the purple band are the S2s, which occur within the $(70,700)$ μs time window after the initial $S1_m$ signal. The pulses outside the two bands are mostly single-electron signals due to photoionization [45].

where $n_{Xe}$ is the number density of xenon nuclei, and $d\sigma_{A,\chi}/dq^2$ is the interaction-dependent differential cross section using the implementation in Ref. [41]. The distance that a MIMP travels inside the liquid xenon before a NR occurs follows the exponential probability of $1/\lambda$. A simulated MIMP track with a random velocity drawn from $f(\vec{v})$ is first determined, followed by simulations of the vertices and time for each NR. The numbers of photons and electrons created in each recoil are modeled following Ref. [42]. The pulses detected by each photomultiplier tube (PMT) from a MIMP event are then simulated by a waveform simulator [43], which models S1s and S2s in the detector. Figure 1 shows an example simulated waveform for a MIMP crossing the TPC. We also simulate the dominant inelastic contribution for SD scattering following Ref. [44]: immediate gamma emissions after the initial nuclear recoils (<1 ns), with energies of 39.6 and 80.2 keV for $^{129}$Xe and $^{131}$Xe, respectively. Since the branching ratio of inelastic scattering is only ~2% for the SD interactions, we find only a percent-level change in the total acceptance of the MIMP signal. The maximum cross section considered in this analysis is limited by the computational challenges in simulating the large number of interactions caused by a passing MIMP. Simulated tracks crossing the top 10 cm of the 96 cm tall TPC were excluded to ensure a minimum of 70 μs time separation between the $S1_m$ and the S2s for best signal identification. This leads to an average MIMP track length of 73 cm in the TPC and a 38% decrease in the total MIMP flux.

We used 219.4 live days of XENON1T data taken during 2017 and 2018 [25], with the full 2 tonne active volume of the TPC. Multiplying the live time by the detector's effective cross-sectional area of 0.86 m$^2$, calculated using a toy Monte Carlo simulation, resulted in a final exposure of 188.7 m$^2$ × day. The data were reprocessed to remove a software limit on the number of photons detected per pulse and kept blinded before all selection criteria were finalized.
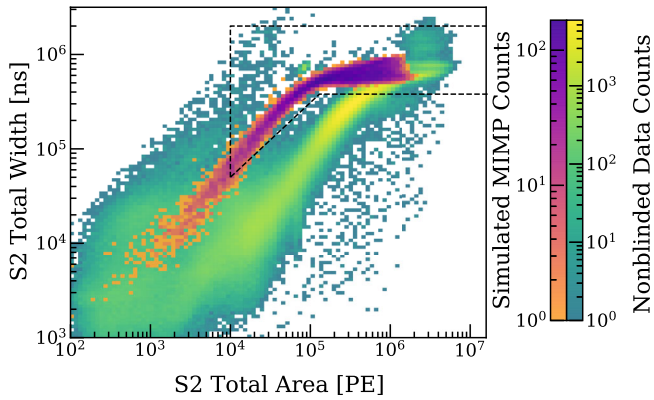
FIG. 2. The total area versus total width distribution for the 4% nonblinded background events (green, yellow) and the simulated MIMP (orange, purple), after applying all other data selections mentioned in the text *except* the $S1_m$ selection in Fig. 3. The selections on total area and total width are defined as the region inside the dashed lines.
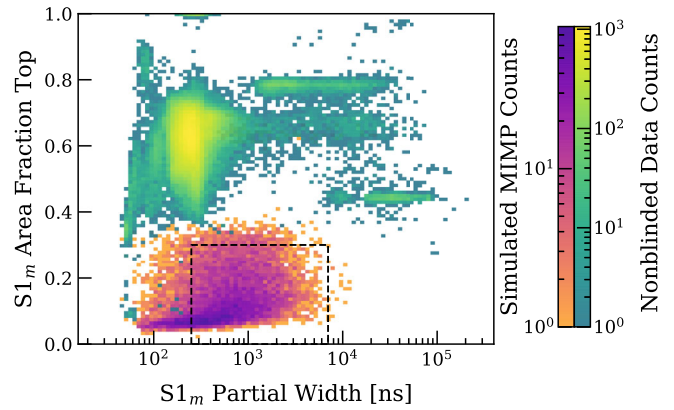


FIG. 3. The partial width versus AFT distribution for the 4% nonblinded background events (green, yellow) and the simulated MIMP (orange, purple), after applying all other data selections mentioned in the text. The $S1_m$ candidate selection is defined as the region inside the dashed square.

However, 4% of the data were not blinded and were instead utilized for validation purposes, in conjunction with the aforementioned simulation, for determining the MIMP selection criteria as follows.

The S2s contribute to the majority of the pulses in a MIMP event. To select the MIMP signal, we use the sum of the integrated pulse *areas*, and the sum of the *widths* (defined as the time difference between the 25%–75% quantile of the pulse area) of these S2s. For the same total area, we expect MIMPs to have a higher total width compared to a single-scatter electronic recoil due to their spread in time. Figure 2 shows the total area versus total width distributions for the nonblinded data and the simulated MIMPs.

The $S1_m$ pulse is a distinctive signal for MIMPs. The "area fraction top" (AFT) is defined as the fraction of pulse area seen by the top PMT array. Prompt scintillation ($S1_m$ or S1) from the liquid xenon gives AFT values below 0.35 due to total internal reflection on the liquid-gas interface, while proportional scintillation (S2) from the gaseous xenon gives AFT values between 0.4 and 0.8. The "partial width" is defined as the time difference between the 10%–50% quantile of the pulse area. The average partial width of the simulated $S1_m$ is 0.8 μs for a MIMP interaction, which is distinctive from the partial widths of the typical S1s (∼0.2 μs) and S2s (∼10 μs) in XENON1T [26]. When combined, the small AFT values and large partial widths provide distinctive signatures for MIMPs, characteristic of their nonrelativistic trajectories through the TPC. We select the first peak above 250 PE that is categorized as a S2 as the potential $S1_m$ candidate. To avoid the background of consecutive radioactive decays, any event with additional S1 pulses above 200 PE is also rejected. Figure 3 shows the partial width versus AFT distributions of the candidate $S1_m$ pulses in both simulation and nonblinded data after all the selections mentioned previously, plus a muon-veto selection on data (discussed below). Only 0.04% of the events in

data have $S1_m$ candidate pulses with AFT values below 0.3, which happens when a single S1 or multiple S1s are misidentified as a S2. We analyze the waveform patterns of those events with $S1_m$ partial widths above 100 ns and identify their origin from the decay chain of the trace amount of $^{220}$Rn within the TPC. In the decay chain, the beta-gamma decay of $^{212}$Bi is followed by the alpha decay of $^{212}$Po after a delay of approximately 200 ns, resulting in their S1 pulses overlapping. $^{222}$Rn can produce a similar signal from the $^{214}$BiPo decays with a rarer occurrence. Since actual MIMPs can have much larger partial widths, observing all MIMP signals with partial widths <250 ns is very unlikely ($p$ value $< 10^{-5}$). To avoid the observed $^{212/214}$BiPo backgrounds and the potential multiple-scattering neutron background, the minimum value of the partial width parameter was chosen to be 250 ns, and the MIMP search region is defined within the dashed lines in Fig. 3.

The cosmogenic muon flux in the underground hall B of LNGS is about 1.2 events/$(m^2 \times h)$ [46,47]. Unlike MIMPs, GeV muons travel at relativistic speeds, producing $S1_m$ pulses with shorter partial widths (<200 ns), which can be vetoed by the aforementioned MIMP selections with >99% efficiency. However, muons that travel through the top of the TPC will produce ionization signals in the gaseous xenon simultaneously with scintillation signals in the liquid. This results in a broader $S1_m$ pulse similar to MIMPs. By utilizing the 10 m water Cherenkov detector surrounding the TPC [46], we implement the muon-veto selection criteria as defined in Ref. [48]. The muon-veto system achieves a 99.5% muon tagging efficiency while only incurring a 1% exposure loss. Prior to unblinding the full dataset, we unblinded all events within 1 μs of a muon-veto trigger, finding ten muon-induced events in the MIMP signal region. This yields a background expectation of 0.05 events attributed to unvetoed muon leakage in the total exposure.
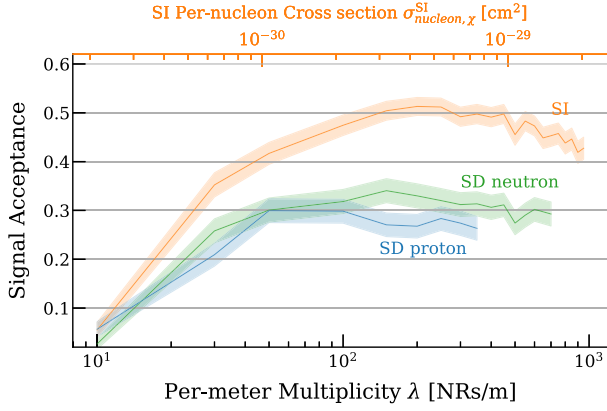
FIG. 4. The signal acceptance of MIMPs with per-meter multiplicity $\lambda$ for applied selection criteria, for SI scattering (orange), SD neutron-only scattering (green), and SD proton-only scattering (blue). The 38% decrease in the MIMP flux due to the top 10 cm veto volume was taken into account in the signal acceptance. The top $x$ axis shows the corresponding MIMP-nucleus SI cross section assuming coherent enhancement. The uncertainty bands denote the 90% Wilson confidence intervals.

The probability of a MIMP signal passing our selection criteria as a function of per-meter NR multiplicity $\lambda$ is shown in Fig. 4, with the corresponding SI MIMP-nucleus cross section shown for reference. The total signal efficiency is driven by the $S1_m$ selection, where MIMPs with short track lengths are rejected due to their similarity with double-S1 backgrounds. The current data-processing algorithm uses "Jenks optimization" [49], which splits a waveform into multiple pulses based on the criteria of minimizing overall deviation. When a MIMP track includes NRs with higher energies ($\gtrsim 70$ keV), the fluctuation in the $S1_m$ waveform becomes more significant. As a result, the partial width of $S1_m$ for MIMPs decreases due to peak

splitting, which in turn reduces the efficiency of finding the $S1_m$ peaks. This effect is more apparent in the SD MIMP-nucleus scattering, as their high-energy recoils occur with a higher relative frequency, leading to a decrease in their signal acceptance.

Upon unblinding, no MIMP candidate events were found that would satisfy the selections. This is in agreement with our total background expectation of 0.05 events in the full exposure. Hence, we derive MIMP exclusion limits following the Feldman-Cousins [50] procedure. The calculation uses the aforementioned MIMP flux and interaction models, as well as the detection efficiency in Fig. 4. We show in Fig. 5 the 90% confidence level constraints on the SI MIMP-nucleon cross section for masses above $10^{12}$ GeV/$c^2$, with and without the assumed $A^4$ enhancement for coherent scattering. Compared to the standard single-scatter search, this analysis extends the mass reach of XENON1T by 1 order of magnitude to $3 \times 10^{17}$ GeV/$c^2$. In the case of $A^4$ enhancement, the limit covers new parameter space spanning an order of magnitude in cross section and 1 order of magnitude in mass. Cosmological and astrophysics boundaries for MIMPs exist from the spectral distortions of the cosmic microwave background [51,52], interstellar gas clouds [53], and DM interaction with Galactic cosmic rays [54]. However, these observations impose upper limits exceeding $10^{-16}$ cm$^2$ on the DM-nucleon (DM-nucleus) interaction when the DM masses surpass $10^{12}$ GeV/$c^2$. We show in Fig. 6 the 90% confidence level constraints on the SD MIMP-nucleon cross section for masses above $10^{12}$ GeV/$c^2$, assuming neutron- or proton-only coupling. We report these results based on the calculations done in Ref. [36] using the median of their structure function, as well as using alternative nuclear models [37,38]. This analysis rules out approximately 2 orders of magnitude in MIMP-neutron (MIMP-proton) cross section, up to a mass of
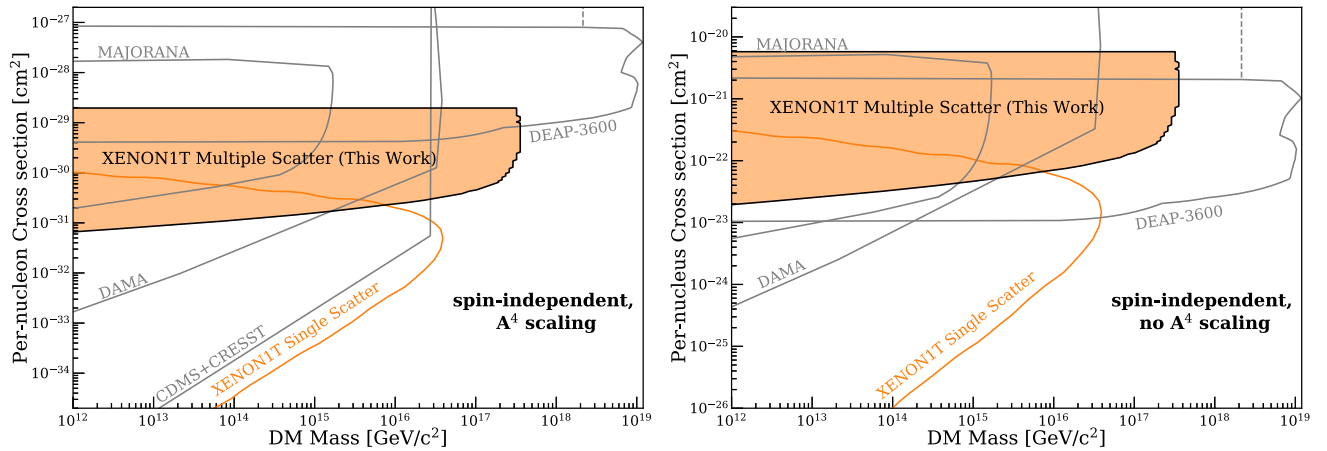


FIG. 5. The XENON1T 90% confidence level constraints on the MIMP spin-independent cross section (orange shaded) from this multiple-scatter analysis, with (left) and without (right) the $A^4$ coherence enhancement. We show the results from the XENON1T single-scatter analysis [23] in the orange line. Other constraints from Majorana Demonstrator [23,56], DEAP-3600 [57] (extrapolation in dashed), DAMA [17,53], and CRESST + CDMS [58] (recast) are shown for comparison.
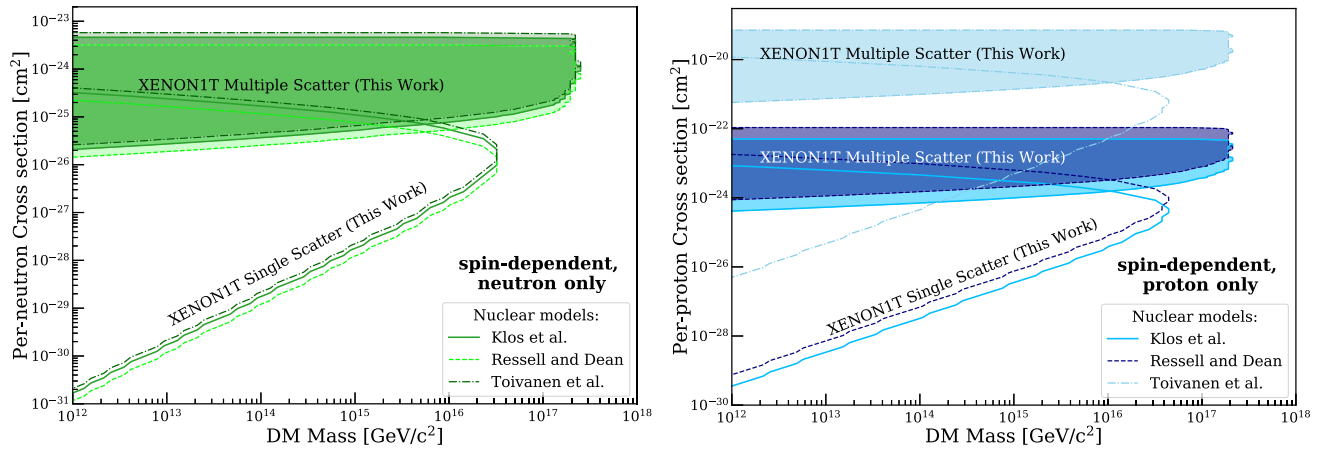
FIG. 6. The XENON1T 90% confidence level constraints on the MIMP-neutron (left, green) and MIMP-proton (right, blue) cross sections. We show the constraints from this XENON1T multiple-scatter analysis (shaded) and a recast of the XENON1T spin-dependent single-scatter analysis [19] (line). Given different theoretical calculations of xenon nuclear models, we show our results based on the works by Klos *et al.* [36] (solid), Ressell and Dean [37] (dashed), and Toivanen *et al.* [38] (dash-dotted).

$2 \times 10^{17}$ GeV/$c^2$. The previous XENON1T single-scatter WIMP results [19] using a 0.65 tonne fiducial mass are recast following the SD MIMP model. Other SD exclusion limits exist but are not shown here: DAMA reported a MIMP-proton limit in 1999 [17], but assumed a structure function of unity; a recent MIMP-proton limit from PICO-60 is derived in a Ph.D. thesis [55].

In summary, we conducted a blind search for tracklike signals from heavy, multiply scattering DM using 219.4 days of data from XENON1T. Following unblinding, we found no signal candidate events and thus calculated exclusion regions for both spin-independent and spin-dependent DM reaching masses up to $3 \times 10^{17}$ and $2 \times 10^{17}$ GeV/$c^2$, respectively. These are the first multiple-scatter constraints set by a xenon-based experiment and the first spin-dependent limits for MIMP-neutron and MIMP-proton interactions. Further sensitivity at even higher cross sections may come from searches using mica slabs [59] or etched plastic [60]. As the DM flux becomes the limiting factor, higher MIMP masses will soon be probed by other liquid noble element detectors that have a larger exposure (measured in area × time). XENONnT [61] and LZ [62] are running and may extend this sensitivity by an order of magnitude in mass, and the upcoming DarkSide-20k [63] and DARWIN/XLZD [64,65] detectors may push this sensitivity beyond the Planck mass. Thus, even Planck-scale physics is within reach of direct DM experiments.

*Appendix: Energy loss from Earth's overburden.*—We used a toy model to simulate MIMPs propagating through Earth's overburden. We modeled the structure of Earth with one spherical core ($r_{\mathrm{core}} = 3480$ km) and two concentric spherical shells of the mantle ($r_{\mathrm{mantle}} = 6347$ km) and crust ($r_{\mathrm{crust}} = 6379$ km), whose chemical components are vastly different. We set up a spherical coordinate system with the center at the TPC (located 1.4 km underground) and the polar angle $\phi = 0°$ pointing toward Earth's center. With an isotropic DM flux, we calculate the distance a MIMP travels in each medium before reaching the underground detector, which depends on $\phi$ but is symmetric in azimuthal angle $\theta$. The total energy loss was calculated for both SI and SD cases using the differential cross section from Eqs. (1) and (2), with the neutron (proton) spin expectation values
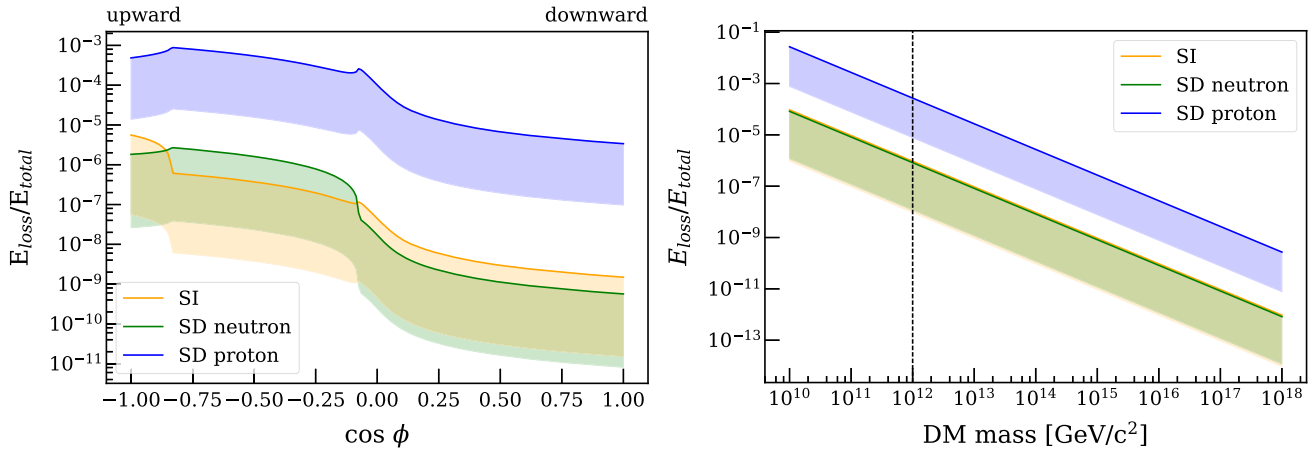
FIG. 7. The fraction of the average kinetic energy loss of MIMPs reaching the underground detector of XENON1T. The solid lines denote the maximum cross sections considered in this Letter, with the shaded areas extending to the minimum cross sections. The left plot shows this fraction as a function of the cosine of the incident polar angle of the MIMP track with a DM mass of $10^{12}$ GeV/$c^2$. The two kinks denote the critical points that MIMP tracks intersect with Earth's mantle and core. The right plot shows the same fraction as a function of the DM mass, averaged over all incident angles. The dashed line denotes the minimum DM mass ($10^{12}$ GeV/$c^2$) considered in this analysis.

$\langle S_n \rangle$ ($\langle S_p \rangle$) taken from Refs. [36,39] and the isotopic abundances and density of different components of Earth taken from Ref. [24]. Note that, for this model, we took the average energy loss for each recoil in the overburden to be $\frac{1}{2} m_T v_\chi^2$ for a conservative estimate, where $m_T$ is the mass of the target nucleus and $v_\chi$ is the DM velocity, which can be approximated as unchanged for small energy loss. Figure 7 shows the fraction of kinetic energy loss for a MIMP with different incident polar angles and masses from our toy simulation. The strongest overburden impact came from the proton-only interaction, given that the proton spin expectation value of xenon is relatively small compared to the ones of the materials in the overburden. To conclude, the MIMP energy loss from Earth's overburden is less than 0.1% for the excluded parameter space in Figs. 5 and 6. This corresponds to a DM mass above $10^{12}$ GeV/$c^2$, and MIMP-nucleon cross section below $2 \times 10^{-29}$ cm$^2$ in the SI case, or MIMP-neutron cross section below $5 \times 10^{-24}$ cm$^2$ and MIMP-proton cross section below $5 \times 10^{-23}$ cm$^2$ in the SD case based on the calculation from Klos et al. [36].

---

*Deceased.
†Also at INFN—Roma Tre, 00146 Roma, Italy.
‡li4006@purdue.edu
§Also at Polytechnic Institute of Coimbra, Coimbra Institute of Engineering, 3030-199 Coimbra, Portugal.
‖Also at Physikalisches Institut, Universität Heidelberg, Heidelberg, Germany.
¶xenon@lngs.infn.it

[1] J. Billard et al., Rep. Prog. Phys. 85, 056201 (2022).
[2] X. Chu, T. Hambye, and M. H. G. Tytgat, J. Cosmol. Astropart. Phys. 05 (2012) 034.
[3] A. Berlin, D. Hooper, and G. Krnjaic, Phys. Rev. D 94, 095019 (2016).
[4] D. J. H. Chung, E. W. Kolb, and A. Riotto, Phys. Rev. D 60, 063504 (1999).
[5] G. F. Giudice, E. W. Kolb, and A. Riotto, Phys. Rev. D 64, 023508 (2001).
[6] A. Azatov, M. Vanvlasselaer, and W. Yin, J. High Energy Phys. 03 (2021) 288.
[7] I. Baldes, Y. Gouttenoire, F. Sala, and G. Servant, J. High Energy Phys. 07 (2022) 084.
[8] F. Takahashi, Phys. Lett. B 660, 100 (2008).
[9] B. S. Acharya, G. Kane, S. Watson, and P. Kumar, Phys. Rev. D 80, 083529 (2009).
[10] D. J. H. Chung, E. W. Kolb, and A. Riotto, Phys. Rev. D 59, 023501 (1998).
[11] Y. Ema, K. Nakayama, and Y. Tang, J. High Energy Phys. 07 (2019) 060.
[12] J. H. MacGibbon, Nature (London) 329, 308 (1987).
[13] J. Maldacena, J. High Energy Phys. 04 (2021) 079.
[14] D. Carney, N. Raj, Y. Bai, J. Berger, C. Blanco, J. Bramante, C. Cappiello, M. Dutra, R. Ebadi, K. Engel et al., arXiv:2203.06508.
[15] M. W. Goodman and E. Witten, Phys. Rev. D 31, 3059 (1985).
[16] M. C. Digman, C. V. Cappiello, J. F. Beacom, C. M. Hirata, and A. H. G. Peter, Phys. Rev. D 100, 063013 (2019); 106, 089902(E) (2022).
[17] R. Bernabei et al., Phys. Rev. Lett. 83, 4918 (1999).
[18] G. Jungman, M. Kamionkowski, and K. Griest, Phys. Rep. 267, 195 (1996).
[19] E. Aprile et al. (XENON Collaboration), Phys. Rev. Lett. 122, 141301 (2019).
[20] D. Baxter et al., Eur. Phys. J. C 81, 907 (2021).
[21] J. Read, J. Phys. G 41, 063101 (2014).
[22] J. Bramante, B. Broerman, J. Kumar, R. F. Lang, M. Pospelov, and N. Raj, Phys. Rev. D 99, 083010 (2019).

[23] M. Clark, A. Depoian, B. Elshimy, A. Kopec, R. F. Lang, and J. Qin, Phys. Rev. D **102**, 123026 (2020).

[24] J. Bramante, B. Broerman, R. F. Lang, and N. Raj, Phys. Rev. D **98**, 083516 (2018).

[25] E. Aprile *et al.* (XENON Collaboration), Phys. Rev. Lett. **121**, 111302 (2018).

[26] E. Aprile *et al.* (XENON Collaboration), Eur. Phys. J. C **77**, 881 (2017).

[27] D. R. Tovey, R. J. Gaitskell, P. Gondolo, Y. A. Ramachers, and L. Roszkowski, Phys. Lett. B **488**, 17 (2000).

[28] M. Freytsis and Z. Ligeti, Phys. Rev. D **83**, 115009 (2011).

[29] R. H. Helm, Phys. Rev. **104**, 1466 (1956).

[30] E. Hardy, R. Lasenby, J. March-Russell, and S. M. West, J. High Energy Phys. 07 (2015) 133.

[31] L. Vietze, P. Klos, J. Menéndez, W. C. Haxton, and A. Schwenk, Phys. Rev. D **91**, 043520 (2015).

[32] A. L. Fitzpatrick, W. Haxton, E. Katz, N. Lubbers, and Y. Xu, J. Cosmol. Astropart. Phys. 02 (2013) 004.

[33] M. Hoferichter, P. Klos, J. Menéndez, and A. Schwenk, Phys. Rev. D **99**, 055031 (2019).

[34] J. Engel, S. Pittel, and P. Vogel, Int. J. Mod. Phys. E **1**, 1 (1992).

[35] J. Menendez, D. Gazit, and A. Schwenk, Phys. Rev. D **86**, 103511 (2012).

[36] P. Klos, J. Menéndez, D. Gazit, and A. Schwenk, Phys. Rev. D **88**, 083516 (2013); **89**, 029901(E) (2014).

[37] M. T. Ressell and D. J. Dean, Phys. Rev. C **56**, 535 (1997).

[38] P. Toivanen, M. Kortelainen, J. Suhonen, and J. Toivanen, Phys. Rev. C **79**, 044302 (2009).

[39] V. A. Bednyakov and F. Simkovic, Phys. Part. Nucl. **36**, 131 (2005).

[40] XENON Collaboration, The pax data processor v6.8.0 (2018), 10.5281/zenodo.1195785.

[41] J. Aalbers, B. Pelssers, J. R. Angevaare, and K. D. Morå, Wimprates (2022), 10.5281/zenodo.7041453.

[42] M. Szydagis, J. Balajthy, G. Block, J. Brodsky, J. Cutter, S. Farrell, J. Huang, E. Kozlova, B. Lenardo, A. Manalaysay, D. McKinsey, M. Mooney, J. Mueller, K. Ni, G. Rischbieter, M. Tripathi, C. Tunnell, V. Velan, and Z. Zhao, Noble element simulation technique (2022), 10.5281/zenodo.6808388.

[43] E. Aprile *et al.* (XENON Collaboration), Phys. Rev. D **99**, 112009 (2019).

[44] L. Baudis, G. Kessler, P. Klos, R. F. Lang, J. Menéndez, S. Reichard, and A. Schwenk, Phys. Rev. D **88**, 115014 (2013).

[45] E. Aprile *et al.* (XENON100 Collaboration), J. Phys. G **41**, 035201 (2014).

[46] E. Aprile *et al.* (XENON1T Collaboration), J. Instrum. **9**, P11006 (2014).

[47] M. Aglietta *et al.* (LVD Collaboration), Phys. Rev. D **58**, 092005 (1998).

[48] E. Aprile *et al.* (XENON Collaboration), Phys. Rev. D **100**, 052014 (2019).

[49] G. F. Jenks, in *International Yearbook of Cartography* (Rand McNally, Chicago, 1967), Vol. 7, pp. 186–190.

[50] G. J. Feldman and R. D. Cousins, Phys. Rev. D **57**, 3873 (1998).

[51] C. Dvorkin, K. Blum, and M. Kamionkowski, Phys. Rev. D **89**, 023519 (2014).

[52] V. Gluscevic and K. K. Boddy, Phys. Rev. Lett. **121**, 081301 (2018).

[53] A. Bhoonah, J. Bramante, S. Schon, and N. Song, Phys. Rev. D **103**, 123026 (2021).

[54] R. H. Cyburt, B. D. Fields, V. Pavlidou, and B. D. Wandelt, Phys. Rev. D **65**, 123503 (2002).

[55] B. Broerman, New ideas for tonne-scale bubble chambers and a search for superheavy dark matter with PICO-60, Ph.D. thesis, Queen's University, Kingston, 2022.

[56] S. I. Alvis *et al.* (Majorana Collaboration), Phys. Rev. Lett. **120**, 211804 (2018).

[57] P. Adhikari *et al.* (DEAP Collaboration), Phys. Rev. Lett. **128**, 011801 (2022).

[58] B. J. Kavanagh, Phys. Rev. D **97**, 123013 (2018).

[59] J. F. Acevedo, J. Bramante, and A. Goodman, arXiv:2105.06473.

[60] A. Bhoonah, J. Bramante, B. Courtman, and N. Song, Phys. Rev. D **103**, 103001 (2021).

[61] E. Aprile *et al.* (XENON Collaboration), J. Cosmol. Astropart. Phys. 11 (2020) 031.

[62] D. S. Akerib *et al.* (LZ Collaboration), Phys. Rev. D **101**, 052002 (2020).

[63] C. E. Aalseth *et al.* (DarkSide-20k Collaboration), Eur. Phys. J. Plus **133**, 131 (2018).

[64] J. Aalbers *et al.* (DARWIN Collaboration), J. Cosmol. Astropart. Phys. 11 (2016) 017.

[65] J. Aalbers *et al.*, J. Phys. G **50**, 013001 (2023).